Research Square

Preprints are preliminary reports that have not undergone peer review.
They should not be considered conclusive, used to inform clinical practice,
or referenced by the media as validated information.

Enhanced Crystal Violet dye degradation using Artemisia plant-based synthesized Indium- doped ZnO nanocomposites under UV- Irradiation

badreddine TOUBAL

b.toubal@univ-alger.dz

University of Algiers Benyoucef Benkhedda

Asma BESSAAD

University of Algiers Benyoucef Benkhedda

Ibtissem BOUSNOUBRA

University of Constantine 3

Khaled CHETTAH

Research Center in Industrial Technologies

Lynda AROUI

University Ferhat Abbas of Setif

Research Article

Keywords: Artemisia vulgaris Extract, In- doped ZnO nanocomposites, photoluminescence, M-H hysteresis loop, Crystal Violet dye, photo-mineralization

Posted Date: July 31st, 2026

DOI: https://doi.org/10.21203/rs.3.rs-9296680/v1

License: This work is licensed under a Creative Commons Attribution 4.0 International License.
Read Full License

Additional Declarations: No competing interests reported.

Enhanced Crystal Violet dye degradation using *Artemisia* plant-based synthesized Indium- doped ZnO nanocomposites under UV- Irradiation.

TOUBAL Badreddine[1,2, a*], BESSAAD Asma[1,2, b], BOUSNOUBRA Ibtissem[3,4], CHETTAH Khaled [5], AROUI Lynda [6]

b.toubal@univ-alger.dz ; the 16-digit ORCID: 0009-0008-8567-3154,
a.bessaad@univ-alger.dz; the 16-digit ORCID: 0009-0008-5788-8596,
ibtissem.bousnoubra@univ-constantine3.dz ; the 16-digit ORCID: 0009-0002-3384-3373,
khaled.chettah@doc.umc.edu.dz ; the 16-digit ORCID: 0000-0002-0312-600X,
lynda.aroui@univ-setif.dz ; the 16-digit ORCID: 0000-0002-7836-9786.

[1] Department of Materials Science, University of Algiers 1 (Benyoucef Benkhedda), Algiers, Algeria.
[2] Laboratory REVIECO, Faculty of Sciences, University of Algiers 1, 16000 Algiers, Algeria.
[3] Department of Process Engineering, Faculty of Process Engineering, University Salah Boubnider Constantine3, 25000 Constantine, Algeria.
[4] Laboratory of Science and Technology Environment, Department of Chemistry, Faculty of Sciences, University of Brother's Mentouri, 25000 Constantine, Algeria
[5] Research Center in Industrial Technologies, CRTI, Algiers, Algeria
[6] Laboratoire d'Energétique Et Electrochimie du Solide (LEES), Université Ferhat, Abbas Sétif 1, 19000 Sétif, Algeria

Abstract: This study demonstrates the Indium- addition effect on the physical properties of ZnO-based nanoparticles as well as its use for the Crystal Violet (CV) photocatalytic activity. For ZnO nanoparticles preparation ends, *Artimisia vularis* extract is used as the green precursor with Zinc nitrate hexahydrate. The Indium-atoms are then introduced into the ZnO at a 5*a*t % concentration using Indium-nitrate salt as a dopant precursor. Consequently, the physical properties of the Indium-doped ZnO (5In-ZnO) nanocomposites are studied. The crystal structure through *X-ray diffraction* and Raman spectroscopy analyses of both prepared pure (P-ZnO) and 5In-ZnO nanoparticles reveal their hexagonal wurtzite configuration. The FTIR spectroscopy analysis confirms the Zn-O functional chemical group for both preparations. The morphological SEM and TEM analyses show a heterogeneous grain shape structure, and an agglomeration character respectively for the 5In-ZnO nanocomposites. The optical properties through the UV-vis absorbance analysis indicate a minimal blue shift accompanied with a band gap reduction energy from 3.24 to 3.22 eV when Indium atoms are being incorporated. Two characteristic emission peaks have been displayed through the photoluminescence (PL) analysis for both preparations where the visible one at 568 nm in the 5In-ZnO is stronger than to that of the P-ZnO located at 566 nm. This observation indicates an increase in the point-defects concentration inducing a weak ferromagnetism for both synthesized nanocomposites. The 5In-ZnO photocatalyst reached 99.9% decolourization of the CV under UV-irradiation after 25 min. The photomineralization has attained 95% based on COD after 300 min of irradiation.

Keywords: *Artemisia vulgaris* Extract; In- doped ZnO nanocomposites; photoluminescence; *M-H* hysteresis loop; Crystal Violet dye; photo-mineralization.

1 Introduction

Addressing the noxious effects of synthetic dye discharge remains significantly challenging to safeguard the aquatic ecosystem. The release of untreated artificial dyes into water bodies frequently causes environmental complications [1]. These effluents contribute to the deoxygenation and reduced light penetration in waters, inducing the asphyxiation, sterility and feminization the of aquatic organisms due to endocrine disruptors compounds [2]. Additionally, the presence of these untreated dyes in the food production chain presents potential risks to human health [3].

The Cristal Violet (hexamethylpararosaniline chloride, CV) is recognised as a basic dye due to its cationic character in solution. It belongs to the triphenylmethane groups. The dye structure consists of a central carbon atom that is linked to three phenyl- rings. This synthetic dye has a wide range of applications across many sectors. It is used to colour goods such as leather, cosmetics, paper and food products [4]. The CV is considered as a critical component in the textile manufacturing [5-4]. The dye is also used as a colour additive in medical, biological, and pharmaceutical contexts [6-5]. The consumption of such dyes is increasingly widespread, hence the need to find an effective solution to reduce their environmental impact should grow exponentially particularly in water bodies [7].

Among the various water treatment strategies, semiconductor photocatalyst nanoparticles, especially zinc oxide nanoparticles (ZnO- NPs). The ZnO has gained a significant attention due to its ability for efficient organic pollutants degradation [8]. ZnO is an n- type semiconductor which is characterized by a direct bandwidth around 3.37 eV and a substantial exciton binding energy of 60 meV. It also exhibits a beneficial thermal and chemical stability as well as possesses piezoelectric and pyroelectric behaviours [9]. These properties consistently prompt researchers to enhance its performance by initiating additional attributes or functionalities.

The literature classifies the ZnO-NPs properties' enhancement into two ways; they either get coupled with other compounds [10- 5] or modified through incorporating dopant elements [2]. Research has explored various doping elements within this context for diverse applications. Illustrations might include doped ZnO –NPs by Fe [11], Ag [12], Cu [13] for medical applications, by Ag [14], Cu [15-16] for biological and environmental applications, by Sn [17] for electronic applications. Researchers have additionally tackled the photocatalytic activity, an advanced oxidation process for dye removal, employing the ZnO nanoparticles doped method. Hence, this purely environmental application includes, but is not limited to, the

following elements doped ZnO nanoparticles: Mg doped ZnO -NPs [18-19], Mn doped ZnO -NPs [20], Mo doped ZnO -NPs [21], Cu doped ZnO -NPs [22-15], Dy doped ZnO -NPs [23], La doped ZnO -NPs [24] and Co doped ZnO -NPs [25].

As already mentioned through examples their exist a large number of dopants, and selecting the appropriate one is to be based on its beneficial doping properties for ZnO and for ending applications. Using indium for doping is one of the selections that significantly enhances the ZnO performance. This Indium doping is proved to alter the electrical characteristics of ZnO [26] and to behave as donor element when is incorporated into it [27-28]. The indium doping for ZnO is also demonstrated to maintain the n- type conducting character with an improvement in its electrical conductivity [29-30]. It has been validated that the indium dopant improves the control of ZnO crystallinity and modifies its optical properties [31-29].

It imports to underline that even if these properties resulting from indium doping remarkably enhance the ZnO- NPs performance, this latter is also confirmed to be influenced by the utilized synthesis method. There exist a variety of synthesising methods of ZnO nanoparticles, namely hydrothermal [32-14], green synthesis [12-20] co-precipitation [33-29], sol-gel [31-26], and sonochemical techniques [34- 9]. Each of these methods presents pros and cons when being used. This work has adopted the green synthesis method regarding the considerable strengths it offers over its insignificant limits.

The green synthesis process is an eco-friendly plant-based synthesis method that checks the required features when any material is being synthesized: durability, sustainability, cost-effectiveness and environmental impact compared to the conventional chemical techniques. Theoretically speaking this approach enables the use of the variety of existing plants and their various anatomical components such leaves, pods, roots, seeds and flowers. In this study, the *Artemisia vulgaris* has been used for synthesising the nanoparticles in question. The reason behind the choice of the authors lays down in its multiple uses due to its double classification (medicinal and ecological) plant type from one hand [35-36]. From the other hand, this plant's role in reducing, capping and stabilizing agents for metal ions leads to better dispersion and smaller particles' size. Hence, the photocatalytic performance improves [37-38].

Under the main purpose of studying the effect of indium addition on physical properties of ZnO-NPs as well as its use for the CV photocatalytic activity, this paper is organized into four sections. An introduction where the components of the study are highlighted starting from the dye removal problem to propose an advanced resolution approach. The second section covers the experimental phase in which the preparation of both pure and indium- doped ZnO

nanoparticles is completed together with handling and discussing the parameters setting for this synthesis and for the photocatalytic performance achievement. The third section tackles the structural, morphological, optical, magnetic properties as well as the photocatalytic degradation of CV dye under UV- irradiation. To conclude, a brief summary of the outputs is brought out.

2. Experimental details

2.1 Preparation of Artemisia vulgaris Extract

An aqueous extract of *Artimisia vularis* was prepraded by dissolving 5g of the dried material in 200 ml of distilled water, yielding a 2.5% (W/V) solution. The mixture was stirred for 30minutes at 70°C for one hour to facilate the extraction of reducing compounds. The resulting solution was subsequently filtered using a Whattman filter paper and a vacuum Pump (N820 Labo Port) to remove particulate matter and other impurities.

2.2 Biosynthesis of pure and In- doped ZnO nanocomposites

Pure ZnO (P-ZnO) and 5at. % Indium- doped ZnO nanoparticles (5In-ZnO) were synthesized via a green plant- mediated route using Zinc and Indium (III) nitrate salts as precursors. For P-ZnO nanoparticles, 2g of Zinc nitrate hexahydrate (Zn(NO3)26H2O) was weighed and poured into a known volume (100 ml) of mixed solution containing (80 ml) of the prepared Artemisia vulgaris extract and (20 ml) of double distilled water. This adequate mass of (Zn(NO3)26H2O) has been selected to obtain the typical extract concentration of 20g per liter (20g/L). Afterwards, the initial pH was subsequently adjusted from 4.3 to 10 by adding a sodium hydroxide solution (NaOH: 0.2M) in gradual increments. This mixed solution was strirred for approximately 2 hours at 70°C until a whitish precipitate formation. This precipitate as washed five times with double distilled water and centrifuged at 4500RPM for a set of five (5 min) minutes long cycles. The resulting precipitate was dried overnight at 80 °C and the dried (P-ZnO) was annealed in an oven at 150°C for 2 hours. However, 5In-ZnO nanoparticles were prepared with indium (In) concentration of 5% via the addition of Indium (III) nitrate $(In(NO_3)_3$ mass of ($m_{In} \approx 40$ mg). The stoichiometric amount of added (In) salt was calculated using the formula: at. % dopant = [n (dopant) / (n (Zn) + n (dopant))] × 100.

Where n (dopant) is the number of moles of the In dopant, and n (Zn) is the number of moles of zinc.

The final samples 5In-ZnO were subsequently subjected to the same drying treatment as the P-ZnO. Finally, all synthesized nanocomposites were finely ground before subsequent characterization.

2.3 Characterization analysis

The P-ZnO and the 5In-ZnO nanoparticles were characterized using a suite of complementary analytical techniques. The structural and crystallographic properties were investigated by XRD on a Siemens D5000 diffractometer employing Cu Kα radiation (λ = 1.540598A°), with data collected over a 2θ range of 20° to 80° and by Raman spectroscopy using a Berker SENTERRA R200-L system with a spectral range of 50- 800 cm-1. To identify chemical functional groups Fourier-transform infrared (FTIR) spectroscopy is employed (using an 8201PC Shimadzu spectrometer from 400 to 4000 cm-1). Furthermore, the morphological characteristics and elemental composition were analyzed by both Scanning Electron Microscope SEM coupled with EDX spectroscopy (SEM-EDX, JEOL JSM 7001F equipped with an Oxford EDX detector) and Transmission Electron Microscopy (TEM: JEOL JEM 2100F). The optical properties of P-ZnO and the 5In-ZnO nanoparticles were characterized using UV-Visible and photoluminescence (PL) spectroscopy. Absorption spectra were acquired with a JASCO V-760 spectrophotometer while emission spectra were recorded using a JobinYvon FLUOROLOG-FL3-11 spectrofluorometer. Magnetic properties at room temperature of the P-ZnO and the 5In-ZnO nanoparticles were measured by the Vibrating Sample Magnetometer (VSM, MICROSENSE EV9).

2.4 Photocatalytic studies

The photocatalytic performance of the P-ZnO and the 5In-ZnO nanocomposites was assessed by degrading Crystal Violet (CV) dye under visible and artificial light (λ =365nm). The experimental protocol includes the following steps. First, the preparation of (CV) dye solution, then the catalysts (P-ZnO = 1g. L^{-1} and 5In-ZnO =1g.L^{-1}) were introduced separately in into the reactor containing the dye solution. After, the resulting mixture was Stirred in the dark for 30 minutes. finally, the samples were collected at determine time after filtration process with (Millipore, 0.45 μm).

The study also investigated the key parameters affecting system efficiency namely: pH, photolysis direct, initial dye concentration and the effect of adding alcohol. The photocatalytic reactions were conducted in the Pyrex photoreactor fitted with 15 W Polychromatic UV lamp (Philips TLAD 15 W/05) operating at 365 nm. The incident radiation intensity as determined to be (0.791 mW/cm2). However, the photocatalytic reactions under visible light were carried out at solar station using Pyrex reactor (40 cm long, 25 cm diameter). The photocatalytic efficiency was assessed using an Evolution 201 UV/Visible spectrophotometer. The obtained spectra are managed by Thermo INSIGHT software.

3 Results and discussion

3.1 X-ray diffraction analysis

Figure 1 displays the XRD pattern of the green- synthesized P-ZnO and the 5In-ZnO nanocomposites. The XRD patterns of both composites clearly show that all peaks located respectively at 2θ = 31.7°, 34.4°, 36.3°, 47.5°, 56.6°, 62.9°, 66.4°, 67.9°, and 69.1° corresponding to the crystallographic planes, (100), (002), (101), (102), (110), (103), (200), (112), and (201), which are characteristic of the hexagonal wurtzite structure of ZnO [15]. It can be also observed from the insert of the XRD that the feature peaks of wurtzite structure in the 5In-ZnO nanoparticles slightly shifted toward minor angle (see the insert figure.1b) with reduction in their intensity peaks. This decrease in the intensity peaks is probably attributable to the lattice distortions caused by the substitution of In^{3+} (0.76A°) ions for Zn^{2+} (0.74A°) ions [26-29]. Furthermore, no detectable diffraction peaks corresponding to In dopant element or its secondary phases are observed.

The microstructure parameters, such as crystallite size (D) together with deformation (ε), the dislocation density (δ) and the bond length (L) of the P-ZnO and the 5In-ZnO nanocomposites were computed based on an intense peak (101) at diffraction angle 36.3°, that are listed in Table 1. All these statements are written respectively in Equations. (1), (2), and (3) [39-40]. form as:

$$D = \frac{0.9\,\lambda}{\beta \cos\theta} \tag{1}$$

Where: D is the crystallite size, λ = 1.5406 Å (wavelength of Cu-K_α radiation), (β) is FWHM, (θ) is Bragg's angle,

$$\varepsilon = \frac{\beta}{4\tan\theta} \tag{2}$$

(ε) is Microstrain in the crystal lattice of P-ZnO and the 5In-ZnO nanoparticles.

$$\delta = \frac{1}{D^2} \tag{3}$$

(δ) is the number of dislocations per unit area in the both P-ZnO and 5In-ZnO nanoparticles obtained by Williamson and Smallman [39].

$$\frac{1}{d^2} = \frac{4}{3}\frac{h^2 + hk + k^2}{a^2} + \frac{l^2}{c^2} \tag{4}$$

Where 'a' and 'c' denote the lattice constants of the wurtzite structure of P-ZnO and 5In-ZnO nanocomposite and (d_{hkl}) is the interplanar distance.

From the above equation (4) we obtain:

$$L = \sqrt{\left(\frac{a^2}{3} + \left(\frac{1}{2} - u\right)^2 c^2\right)} \tag{5}$$

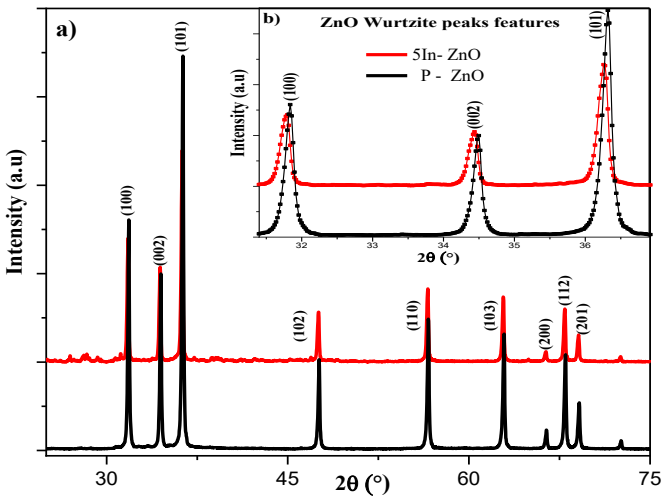
Where: (L) is the bond length of Zn-O in both P-ZnO and 5In-ZnO nanocomposites, (u) is the relative displacement of the anion (O^{2+}) along the c-axis within the tetrahedral coordination, the bond length values are presented in Table.2.

Table 1 crystallite size (D), microstrain (ε), dislocation density (δ) and bond length (L) of the green synthesized P-ZnO and 5In-ZnO nanoparticles derived from using *X*-ray diffraction (XRD) analysis.

XRD calculated analysis of the green synthesis P-ZnO and 5In-ZnO nanoparticles							
Nanocomposite Samples	Lattice parameters(°A) *a*=b	**c**	**c/a**	D (nm)	**ε**(10^{-3})	**δ**10^{14} lines/m^2	**Zn–O**bond length L(Å)
P-ZnO	3.242	5.202	1.604	57.300	1.420	3.050	1.976 - 1.993
5In-ZnO	3.244	5.198	1.602	53.100	1.550	3.550	1.957- 1.992

As can be seen in Table 1, the change in lattice parameter values, and the decrease in crystallite size (D) in the 5In-ZnO nanocomposites compared to the P-ZnO one, can probably correlated to both the incorporation of the In^{3+} ions into the ZnO lattice and in the creation of a relatively new nucleation center. This latter has been extensively validated to be produced in chemical solution synthesis in the presence of In atoms [41]. This behavior was also observed in Ni doped ZnO and Mg doped ZnO nanoparticles [41]. In addition, the obtained results suggest that In- atoms have an impact on the bond length of Zn-O, which can be correlated to the change in covalent band character. The band becomes more covalent that tend to affect the electrical and optical properties of ZnO nanoparticles [15- 42].

Fig 1 XRD patterns of the P-ZnO and the 5In-ZnO nanoparticles synthesized by using *Artemisia vulgaris* extract. The insert (b) is the enlarged view of ZnO Wurtzite peaks features for both P-ZnO and the 5In-ZnO nanocomposites.



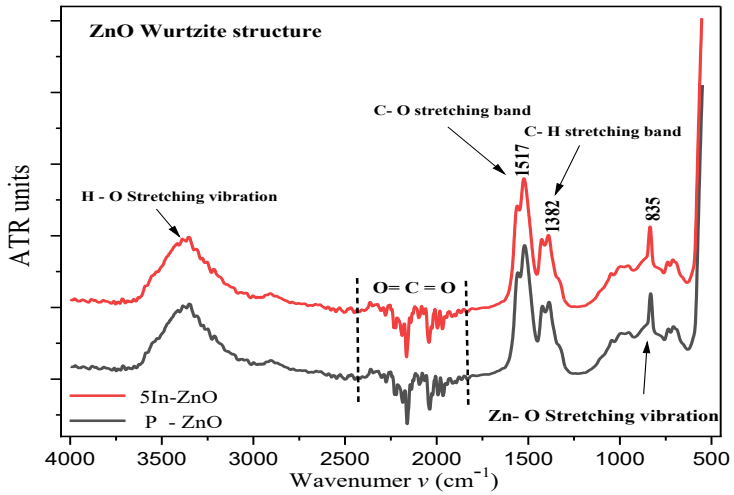
3.2 FTIR spectroscopy analysis

The ATR spectra of the P-ZnO and the 5In-ZnO nanoparticles are plotted in absorbance mode and their traces are presented in figure 2. The ATR spectra of both nanoparticles exhibit similar absorption features of wurtzite ZnO crystal. The first peak observed at 835 cm^{-1} below 1000 cm^{-1} in the P-ZnO and the 5In-ZnO nanoparticles are assigned to bridging zinc-oxygen stretching vibrations of O-Zn-O and Zn-O-Zn in ZnO crystal [43]. Whereas the characteristic absorption bands appeared respectively at 1382 $cm^{-1}$and 1517 cm^{-1} corresponding to the stretching vibrations of carbonyl (CO) and alkyl groups (CH) [44-45]. The large absorption band located approximatively at 3349 cm^{-1} is ascribed to the presence of hydroxyl group –OH adsorbed on ZnO surface [46-43]. No absorption bands corresponding to the indium oxide in ATR spectrum of the 5In-ZnO nanoparticles are observed which probably indicate that this small amount of (5*at*. %) indium occupy substitutional lattice sites into ZnO networks. The principal chemical functional groups (Zn-O stretching band) and the main vibrational (E_2 ^{high}) mode of both the P-ZnO and the 5In-ZnO nanoparticles that are assigned from both FTIR and Raman spectra are gathered in Table 2.

Table 2 Comparative spectroscopic characterization of both green synthesized the P-ZnO and the 5In-ZnO nanoparticles: Vibrational and Optical properties.

	Spectroscopic analysis of the green synthesis P-ZnO and 5In-ZnO nanoparticles				
	VibrationalModeCharacteristics		*Optical Characteristics*		
Nanocomposite samples	Raman Shift (cm^{-1}) E_2 $^{(high)}$ O-Zn	FT-IR bands (cm^{-1}) Zn-O band	PL band emission UV-	Visible-	Optical band gap E_g (eV)
P-ZnO	437.76	834.89	381. 97 nm	566 nm	3.24
5In-ZnO	437.16	835.23	384. 65 nm	568nm	3.22

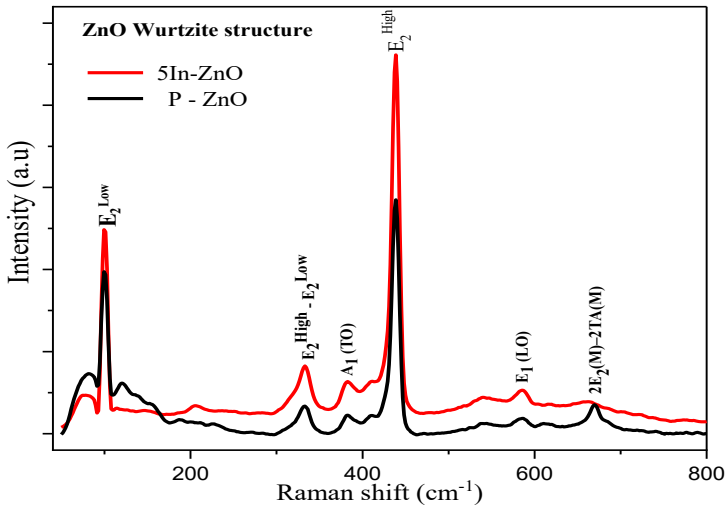
Fig 2 FTIR spectra of P-ZnO and the 5In-ZnO nanoparticles synthesized by using *Artemisia Artemisia vulgaris* extract.



3.3 Raman spectroscopy analysis

Figure 3 shows the Raman spectra of P-ZnO and 5In-ZnO nanoparticles. It is evident that Raman spectra of both nanocomposites display vibrational mode peaks matching those of wurtzite structure of ZnO. These prominent peaks are positioned respectively at 99cm^{-1}, 331 cm^{-1}, 380 cm^{-1},437cm^{-1}, 574 cm^{-1} and 686 cm^{-1}. The bands due to Zinc (Zn) and oxygen (O) atoms vibration are respectively located at 99 cm^{-1} (E_2 ^{Low}) and at 437cm-1(E_2 ^{High}). These two phonon modes are non-polar modes that are activated in Raman spectroscopy. They are indicative of sublattice behavior of both atoms Zn and O in ZnO crystal [15 -26, 47]. The relatively small peaks at 380 cm^{-1}and 574 cm^{-1} are respectively attributed to the actives transversal A_1(TO) and longitudinal optical A_1(LO) modes. These vibration modes indicate that the Zn and O atoms vibrate symmetrically along the C- axis of wurtzite hexagonal crystal of ZnO in both parallel and perpendicular vibration [29-30, 41]. Whereas, the peak located at 331 cm^{-1} is assigned to the (E_2^{High} - E_2^{Low}) difference mode, confirming the good crystallization of ZnO wurtzite structure [41-31]. While the peak at 686 cm^{-1}is attributed to the second order mode combination ($2E_2$(M)–2TA(M)) [44-47]. It can be also observed that when In- is introduced into ZnO lattice the intensity of both peaks (E_2 ^{Low}) and (E_2 ^{High}) increase. This enhanced peak intensity can indicate an enhancement in the crystallinity of ZnO. It also states that the substitution of In^{3+} ions for Zn^{2+}ions in the wurtzite structure is possible. It has already been reported that the increase in the (E_2 ^{High}) peak was also observed in the case of Al- doped ZnO [48]. Moreover, the Raman peaks do not match with those of In_2O_3 and/or In-O-Zn composites in the selected vibrational range of 100-800 cm-1 what perfectly correlates with the already mentioned both XRD and FTIR results.

Fig 3 Raman spectra of P-ZnO and the 5In-ZnO nanoparticles synthesized by using *Artemisia Artemisia vulgaris t* extract.

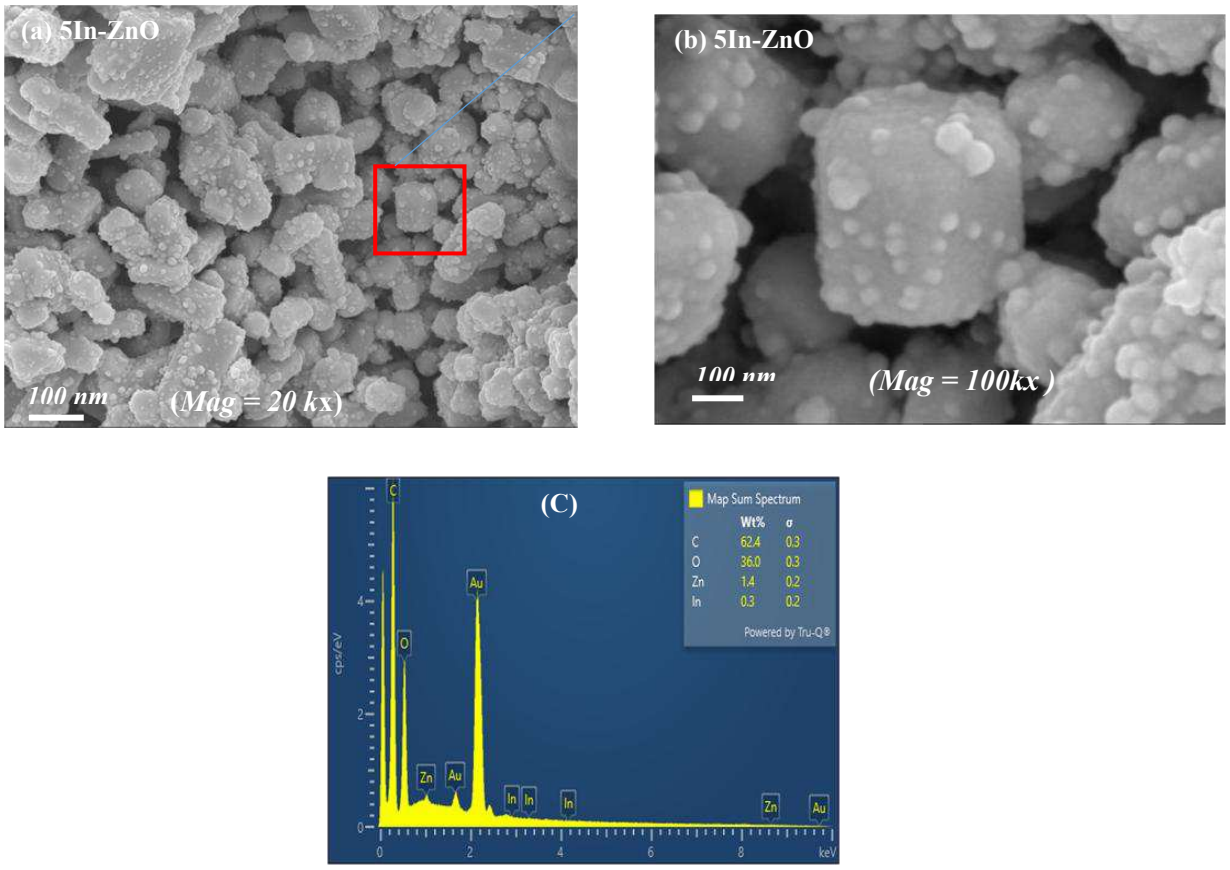


3.4 Morphology observation

3.4.1 SEM and chemical analysis by EDX

Figure 4 shows only the SEM images of the green- synthesized 5In-ZnO nanoparticles obtained respectively at two magnifications (20kx and 100kx). The left micrograph in figure.4 reveals that the microstructure of the 5In-ZnO is composed of agglomerated particles with varied shapes and sizes. However, the right micrograph is a magnified view of the same 5In-ZnO, revealing a mixture of polyhedron, elongate and flat grain form, with small embedded spherical morphology that makes the surface rougher. This structure also exhibits a porous network, a morphology that indicates different degrees of particle growth and aggregation during the synthesis processing. In addition, the atomic concentration (*a*t. %) of constituent elements within the 5In-ZnO nanoparticles were quantified by EDX analysis and their traces are provided in figure 4c. The EDX spectrum shows that all the constituent elements of 5In-ZnO nanoparticles like Zn, O and In are present.

Fig 4 SEM **i**mages of the 5In-ZnO nanocomposites at two magnifications: (a) the left at 20k*x* and (b) the right at 100k*x*. (C) presents the EDX spectrum analysis of 5In-ZnO nanocomposites obtained by using *Artemisia vulgaris* extract.

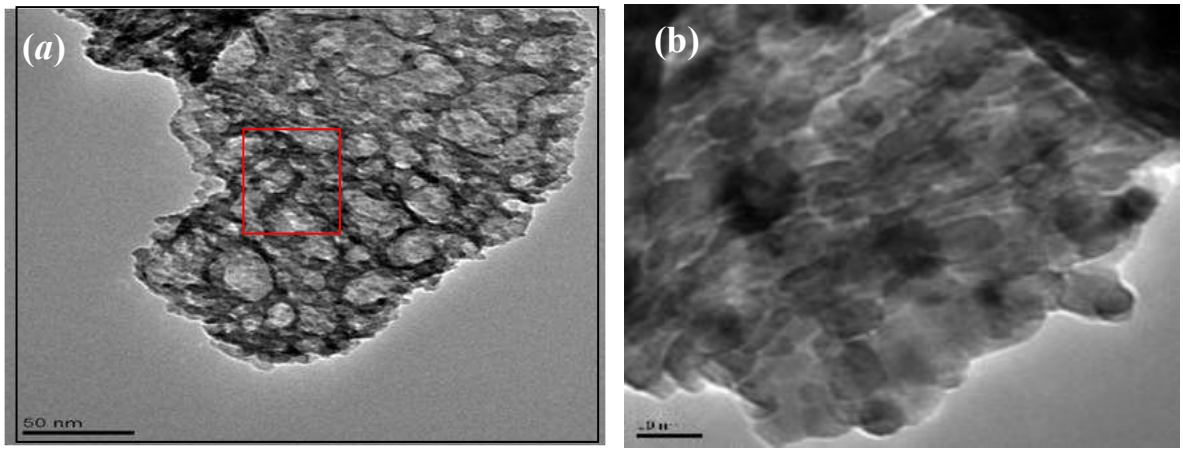


3.4.2 TEM analysis

The Transmission Electron Microscopy (TEM) was employed to investigate the morphological and structural characteristics of the green- synthesis 5In-ZnO nanocomposites

at two different magnifications. As illustrated in figure.5 the left image reveals agglomerated ZnO particles with a heterogeneous distribution. The higher magnification TEM imaging (right) of the 5In-ZnO reveals irregular agglomerates of quasi- spherical and slightly elongated particles, which is consistent with the SEM finding. The size of these agglomerates can range from 20 to 50 nm.

Fig 5 TEM images of he 5In-ZnO nanocomposites at two magnifications: the left (a) at 50nm and the right (b) at 20nm.



3.5 Optical properties by UV-spectrophotometry

The optical properties of the green- synthesized P-ZnO and 5In-ZnO nanoparticles are mainly based on absorption spectra and provided in Figure. 6. It can be observed that the absorption spectra of both P-ZnO and 5In-ZnO display weak absorption in the visible region with a rapid increase in absorption below 395 nm. This increase is related to the exitonic transition [49]. The spectrum of 5In-ZnO nanoparticles also display a slight shift towards shorter wavelengths, indicating the occurrence of the blue shift phenomenon in comparison to the P-ZnO. This bleu shift alters the optical transition by introducing a change in the electronic state of ZnO within the bandwidth, caused by the introduction of shallow energy levels [29-30]. In essence, reducing band gap in the 5In-ZnO nanoparticles can significantly enhance the light absorption and generate more exiton (e-/h+), which probably leads dye degradation enhancement.

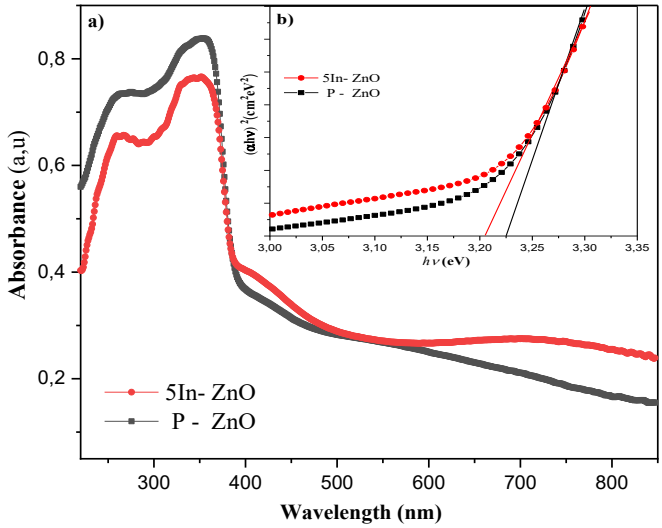
The optical band gap of both the P-ZnO and the 5In-ZnO was calculated using the Tauc formula from the absorption spectra. (Eq. 7) [50-15]:

$$(\alpha h\nu)^{1/2} = C(h\nu - Eg) \quad (6)$$

Where C is a constant, E_g is the energy bandgap, α is the absorption coefficient, and (hν) the photon energy and h the Plank's constant. The value of (1/2) denotes the indirect electronic transition for direct band gap of ZnO.

As can be seen from the insert Figure.6b, the effective absorption edge in the absorption spectra slightly shifts to longer wavelength, which can be ascribed to reduction in the bad gap. The computed band gap values were 3.24 and 3.22 eV for the P-ZnO and the 5In-ZnO nanocomposites, respectively. This moderate reduction in band gap of 5In-ZnO is probably correlated to the defect states formation such as Zn interstitial (Zn_i), Zn vacancies (V_{Zn}), Oxygen vacancies (V_O), Oxygen interstitial (O_i) and thereby would create discrete energy states within the band gap [51]. The substitution of In^{3+} by Zn^{2+} in ZnO lattice introduces discrete, no interacting donor energy states [52], which promote better photocatalytic activity of Indium doped ZnO nanoparticles.

Fig 6 Absorbance spectra of the P-ZnO and the 5In-ZnO nanoparticles. The insert (b) is the Tauc plots for indirect band gap (E_g) of the prepared P-ZnO and the 5In-ZnO using *Artemisia vulgaris* extract.



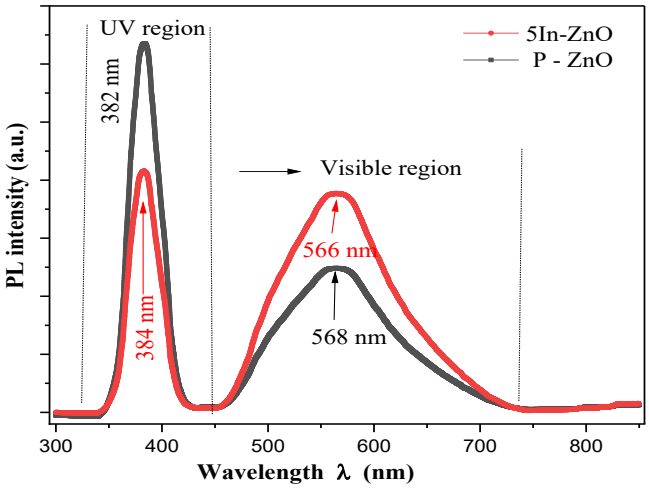
3.6 Optical properties by PL-spectrophotometry

The photoluminescence (PL) spectra of both green-synthesized P-ZnO and the 5In-ZnO nanoparticles were measured and their traces are provided in Figure. 7. It is evident that both PL spectra are characterized by the presence of two main emission peaks. In the case of the P-ZnO nanoparticles, the relative sharp peak that is located in the ultraviolet (UV) region with an emission wavelength at 382 nm is attributed to the band transition of P-ZnO [49-53]. While the broad peaks that spread from 450 to 750nm in visible region with an emission wavelength at 566nm is typically attributed to the presence of intrinsic defects in the crystal lattice of ZnO [41-53]. Likewise, the PL spectrum of 5In-ZnO nanoparticles exhibit a consistent shape appearance when In- is incorporated into the ZnO lattice. The least intense peak, centred at 384 nm can be also attributed to the band transition due to excitation of excess carries in ZnO.

Whereas, the large peak extending from 450 to 750 nm is ascribed to the presence of the intrinsic defect and the impurity atom of indium in the framework of ZnO [44-49] (see Table 2).

According to our finding, the introduction of Indium in ZnO crystal is associated with two effects. The decrease in the intensity of the UV band emission in one hand and the increase in the intensity of the visible band emission in the other hand. First, consider the diminution of intensity in PL spectrum of the 5In-ZnO nanocomposites, which is probably correlated to reduction of recombination process. This latter occurs when electrons and holes are annihilated within the band gap of ZnO. However, the increase in the intensity of the visible band emission in PL spectrum of the 5In-ZnO may be due to an increase in density of point defects such as Zn interstitial (Zn_i), Zn vacancies (V_{Zn}), Oxygen vacancies (V_O), Oxygen interstitial (O_i). These point lattice defects could generate discrete energy states within the ban gap of ZnO structure [51]. In addition, when In- atoms are introduced, they replace Zn atoms in the lattice, resulting in a distribution of new allowed energy states that acts as a trap for the photo- generated carriers (e-/h+ pairs). This incorporation of Indium into crystal lattice of ZnO can generate extra carriers and form efficient recombination centers that probably enhances the photocatalytic efficiency of 5In-ZnO nanocomposites.

Fig 7 Photoluminescence spectra of the P-ZnO and the 5In-ZnO nanoparticles obtained by using *Artemisia vulgaris* extract.



3.7 Magnetic properties of nano composite

Figure 8 shows the measured M-H curves of the green- synthesized P-ZnO and 5In-ZnO nanoparticles, taken by VSM at room temperature. It is worth noticing that the magnetic field (B) was oriented parallelly (B‖) to the nanoparticles surface. The appearance of the M-H hysteresis loop indicates that both synthesized nanoparticles exhibit a weak ferromagnetic behavior at room-temperature. It is also clear from figure 8 that the M--H hysteresis loop is closed that means both the P-ZnO and the 5In-ZnO nanoparticles return to their original

magnetic state indicating the reversible magnetic character. The values of remanent magnetization (Mr) and saturation magnetization (Ms) for P-ZnO are 0.0018 emu/g and 0.0343 respectively. While for 5In-ZnO nanoparticles, they are 0.0025 emu/g and 0.0429 emu/g respectively (see Table3).

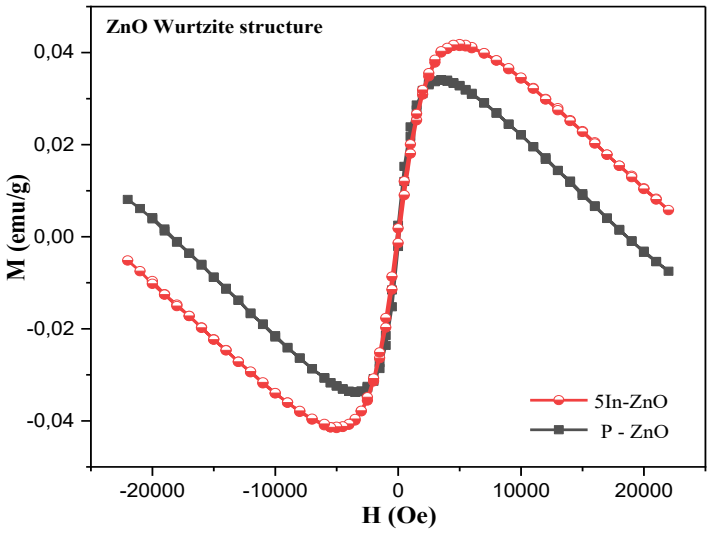
Table 3 Magnetic parameters of the green synthesized P-ZnO and 5In-ZnO nanoparticles at room temperature.

	Magnetic properties of the green synthesis P-ZnO and 5In-ZnO nanoparticles		
Nanocomposite samples	Saturation field (10^2 Oe)	Ms (emu/g)	Mr (emu/g)
P-ZnO	34.88	0.0343	0.0018
5In-ZnO	50.84	0.0429	0.0025

The observed ferromagnetic character of non-magnetic metal oxide materials such as hafnium dioxide (HfO_2) [54], titanium dioxide (TiO_2) [55], zinc oxide (ZnO) [56], cerium dioxide (CeO_2) [56], and tin dioxide SnO_2 [57] is well documented in the literature and is ascribed to the presence of point defects in their crystal lattices. The presence of the oxygen defects (V_O) is mainly introduced trap levels in the crystal of these non-magnetic metal oxide materials. These trapped electrons subsequently can interact with localized spin polarized states that create an exchange coupling between adjacent magnetic moments. However, when In-atoms are introduced as foreign atoms into ZnO structure the magnetic hysteresis curve is also observed.

The role played by In^{3+} ions incorporated in ZnO structure is to maintain the n-type semiconductor character by generating more electrons. This type of impurity can also produce different effect such as broken chemical banding and alter the periodicity in the atomic arrangement into ZnO crystal, which tends to modify its defect density by increasing oxygen vacancies and thereby modify its magnetic behavior. In addition, using plant extract to synthesize the biogenetic samples can promote a high defect concentration of oxygen vacancies, which affects the occurrence of room temperature ferromagnetic properties [57].

Fig 8 M-H curves of the P-ZnO and the 5In-ZnO nanoparticles obtained by using *Artemisia vulgaris* extract at room temperature.

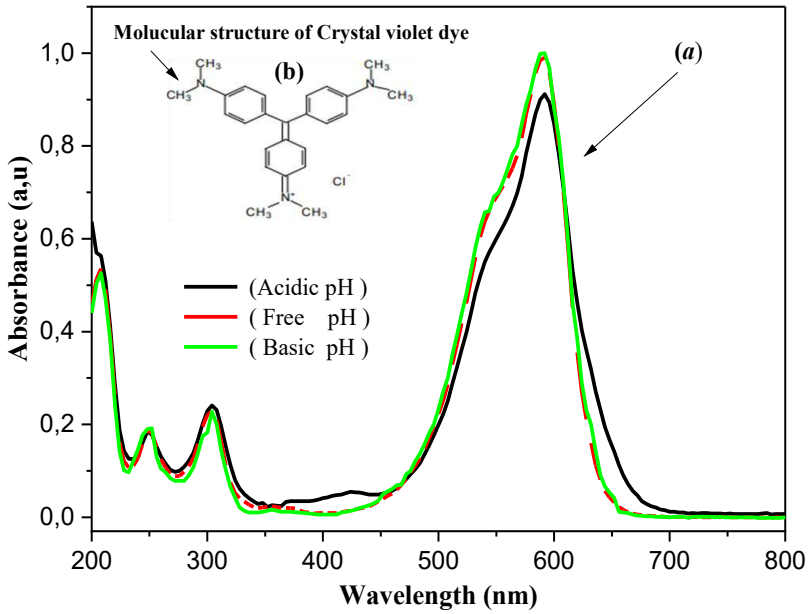


3.8 Photocatalytic analysis of In- doped ZnO nanocomposites

3.8.1 Influence of pH medium

Figure.9 shows the absorption spectra of the CV dye at different pH levels (figure.9a), and the insert (figure.9b) is the molecular structure of the CV dye. It is evident that the mean absorption peak of the CV dye, located approximatively at 592 nm remains constant in the wavelength range of 200-800 nm. When the pH solution changes from basic to acidic there is no significant shift in the main peaks of CV dye. This can probably be related to the stability of electronic structure of chromophore and its ability to absorb similarly at that wavelength [58 - 59].

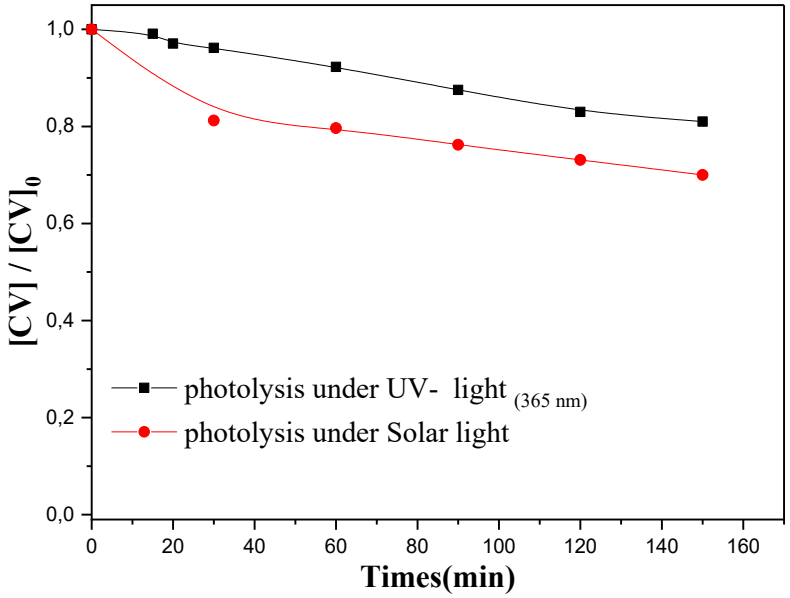
Fig 9 The absorbance spectra of Crystal Violet (CV) in different medium solution. The insert (b) presents the structure of CV dye molecule used as target organic pollutant.



3.8.2 Direct photolysis of CV dye

The direct photolysis of the CV dye by 5In-ZnO nanocomposites under artificial light (λ =365nm) and under solar light are presented in figure 10. It can be observed that the degradation process under solar radiation is more significant compared to artificial light (UV-λ =365nm). After 150 minutes of exposure, the (CV) degradation rate is 19% under artificial light, while it reaches 30% with sunlight. This low degradation rate under both light sources is probably ascribed to the low contribution of photons emitted by both sources, sunlight and UV-irradiation, necessary to initiate effective photolysis reactions.

Fig 10 Comparative study of photolysis directs of the CV under solar and artificial light at λ equal 365nm.

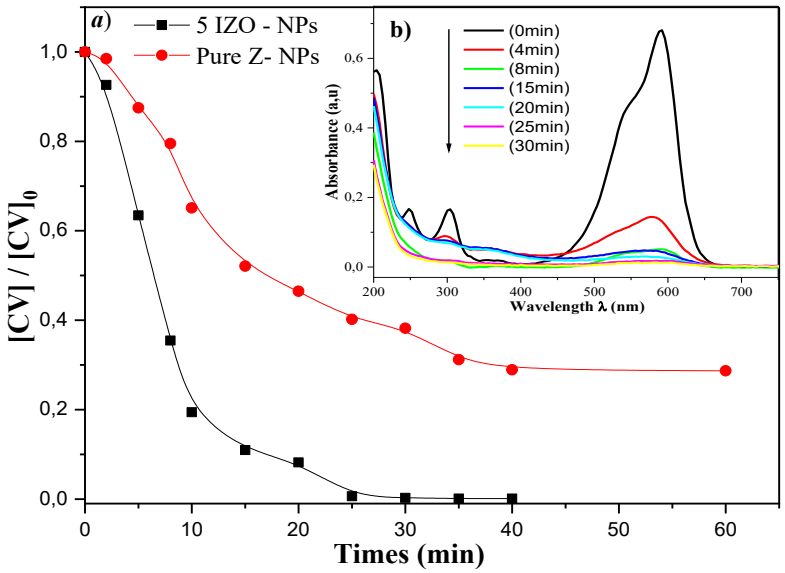


3.8.3 Kinetics of the CV degradation

Figure.11 depicts the photocatalytic degradation kinetics of the CV dye (figure 11a) and the insert (figure.11b) is the corresponding absorbance spectra of the CV, only in the presence of [(5In-ZnO = 1g. L^{-1}) under UV- light irradiation (λ = 365 nm)]. The reaction kinetics indicate that near complete degradation is achieved only after 25 minutes of treatment with 5In-ZnO nanocomposites, whereas the P-ZnO [at the same experimental conditions (P-ZnO =1g. L^{-1}) under UV- light irradiation (λ = 365 nm)] reach only 72% even after 60 minutes of treatment. The improvement of reaction rate is probably attributed to enhanced separation of photo-generated carriers (e^-/h^+ pairs) accelerated by Indium addition [60-61]. Furthermore, the incorporation of In^{3+}ions into the ZnO lattice tend to increase the carrier (e-/h+ pairs) concentration [62-63], extend light absorption [64-65] and promote the formation of reactive

radicals (hydroxyl •OH) [61-62], which confirmed the superior photocatalytic reaction of 5In-ZnO nanocomposites.

Fig 11*a* is the kinetics photodegradation for CV in the presence of P-ZnO (●) and 5In-ZnO (■) nanoparticles. The insert (Fig 11b) is the absorbance spectra of the CV in the presence of 5In-ZnO-NPs = 1g. L^{-1} under UV light irradiation at λ equal 365nm.



3.8.4 Influence of the initial CV concentration

The effect of initial dye concentration on the photocatalytic decolorization of the CV was estimated under the following selected experimental conditions (free pH, ambient T=20°C, 5In-ZnO dose of 1g. L^{-1} and under UV- light irradiation (λ = 365 nm)). From figure12a, it appears that the photocatalytic activity of the CV occurred more rapidly at lower dye concentration. The degradation of the CV dye reached 99,9%, 91,10% and 89,05% for initial concentrations of 10, 15, and 20 ppm respectively, demonstrating a high removal rate within a short UV irradiation time of 25 minutes. This result is ascribed to the development of photo-generated species such as (hydroxyl •OH), (superoxide anions $O_2^{\bullet-}$) and (holes h^+) that interact with the CV dye molecules. Otherwise, the photo-generated species are reduced on the activate sites of 5In-ZnO nanoparticles.

The kinetics of photocatalytic degradation of the CV match well with the Langmuir-Hinshelwood (LH) kinetic model that was applied to delineate the effect of initial dye concentration as a function of irradiation time. This kinetic model can be expressed as (Eq.7).

$$\mathrm{Ln}\left(\frac{C_0}{C_t}\right) = K_{app}\, t \qquad (7)$$

Where C_0 and C_t are the CV solutions concentration before and after exposure to UV-light for 60 minutes respectively and Kapp is the pseudo-first order rate, represents the slope of the linear plot in the insert figure 12b.

Furthermore, the half time ($t_{1/2}$), defined as time required for 50% degradation of CV, was calculated by Eq.8

$$\mathbf{t_{1/2}} = \ln 2/k \qquad (8)$$

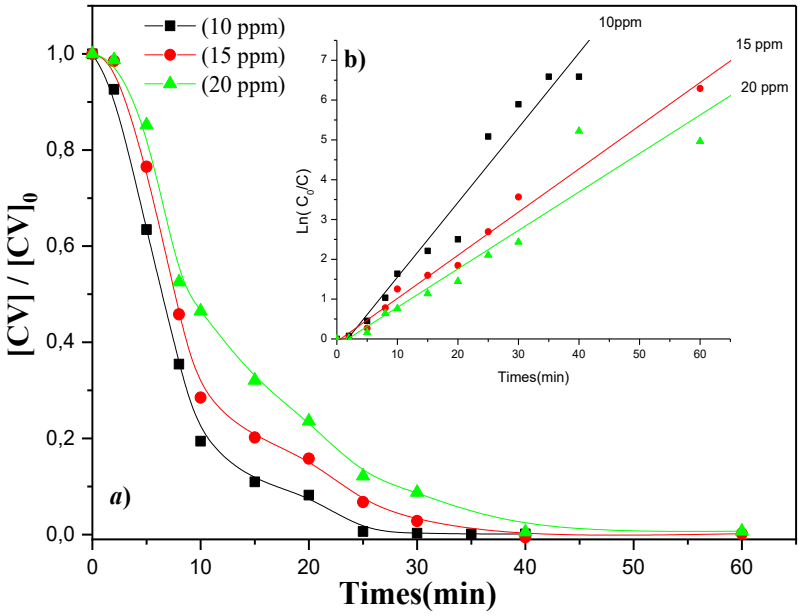
The photocatalytic activity parameters including the percentage dye degradation (%), Rate constant (kapp), half-life values and the coefficient of determination (R^2) for CV degradation at various initial CV concentrations are listed in Table 4.

Table 4 Photdegradation efficiency (%), Rate constant ($\mathbf{k_{app}}$), half-life values and the coefficient of determination (R^2) for CV degradation at various initial CV concentrations in the 5In-ZnO nanocomposites under UV- light irradiation (λ = 365 nm)

[CV] ppm	Photdégradation efficiency (%)	$t_{1/2}$(min)	R^2	k_{app} (min^{-1})
10	99,90	6.37	0,96383	3,73 10^{-1}
15	91,10	7.54	0,96729	2,53 10^{-1}
20	89,05	9.13	0,97699	1,79 10^{-1}

In fact, from Table 4 is reckoned that the degradation rate of the CV decreased from 99,9% to 89,05% as the initial concentration increased from 10 to 20 ppm with an excellent linear correlation ($R^2 > 0.95$) corroborating the first- order kinetic model.

Fig 12a shows the influence of the initial CV concentration on the photocatalytic degradation efficiency: 5In-ZnO = 1g.L^{-1}, free pH and at T = 20°C. The insert (fig 12b) presents the linearization of kinetics reaction model applied to decolorization of the CV.



3.8.5 Influence of alcohol addition

The role of photo-generated species, particularly the hydroxyl radical (•OH) in the photocatalytic process, was assessed by adding 2% of tert-Butanol into the reaction medium comprising the CV dye solution (10 ppm) in the presence of 5In-ZnO =1g. L^{-1}. the obtained results are illustrated in figure 13 and demonstrate that the degradation activity of the CV dye decreases from nearly complete removal 99.9% to 78% in the presence of 2% of tert-Butanol after 25 minutes of UV light -irradiation (λ = 365 nm).

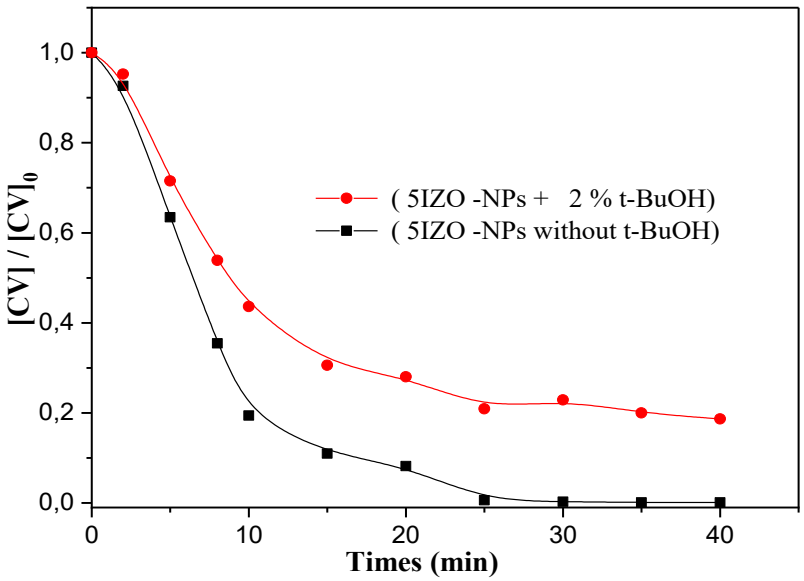
The decrease of the CV photocatalytic activity by scavengers was computed using Eq.9 [66].

$$\text{Inhibition } (\%) = \frac{(V)_{max} - (V)_{min}}{(V_{max})} . 100 \qquad (9)$$

Where $(V)_{max}$ is the maximum rate (0% tert-butanol) and $(V)_{min}$ is the minimum rate (2% tert-butanol).

It is well established that a lower concentration of hydroxyl radicals (•OH) trapped by tert-Butanol on the surface of 5In-ZnO nanocomposites, implies reduced oxidative power that usually results in diminished degradation activity of the CV dye [58-60]. Hence, the hydroxyl radicals (•OH) play a significant role in the photocatalytic activity of the CV dye.

Fig 13 Influence of alcohol addition of tert- butanol on the photocatalytic degradation efficiency of (CV = 10 ppm) in the presence of 5In-ZnO = 1g. L^{-1}, free pH, at T = 20°Cand under UV light irradiation at λ equal 365nm.

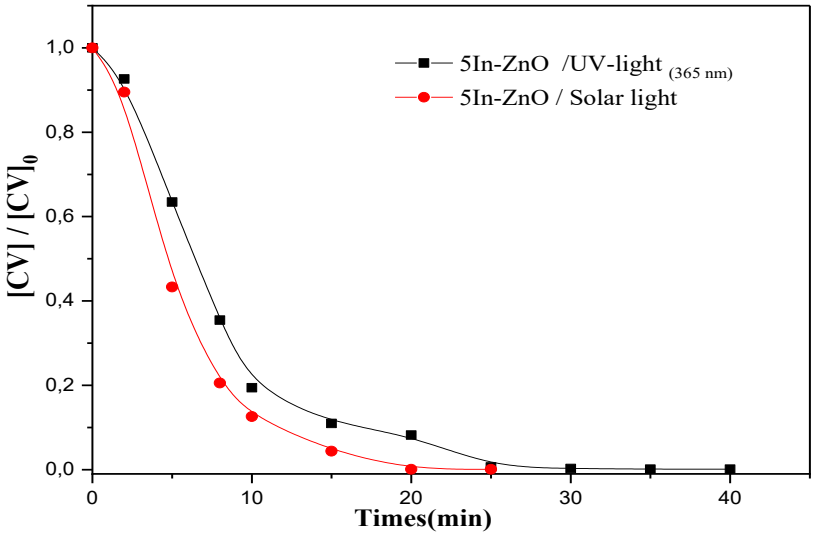


3.8.6 Solar photocatalytic degradation of Crystal violet (CV)

Figure 14 displays a comparison of the CV photocatalytic activity under sunlight and UV light (λ = 365 nm). To achieve the adsorption equilibrium, a suspension of 1 $g.L^{-1}$ of the

5In-ZnO nanoparticles was kept in the dark for 30 minutes. It is apparent that the photocatalytic activity of CV is effectively faster under naturel light, attaining nearly complete removal within only 20 minutes, compared to artificial UV light (λ = 365 nm), which reaches only 90% degradation over the same irradiation times. The data indicate that the degradation rate of CV is strongly influenced by the nature of radiation employed. Furthermore, varying the energy source could potentially alter both the mechanism and the rate of photocatalytic treatment.

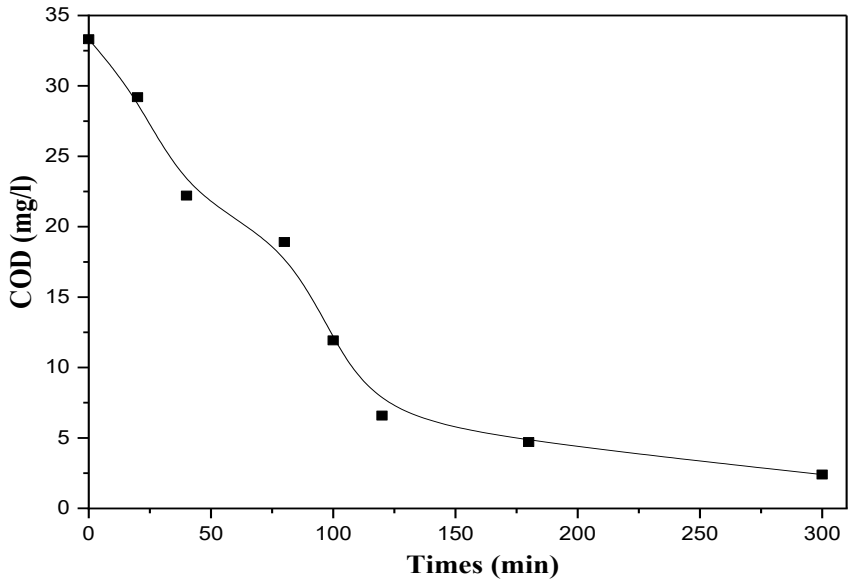
Fig 14 Comparative kinetic analysis of Crystal Violet degradation (CV = 10 ppm) in the presence of 5In-ZnO = 1g. L^{-1} under solar (●) and artificial light at λ equal 365nm (■).



3.8.7 Mineralization of Crystal violet (CV)

The photo-mineralization efficiency of the Crystal Violet (CV) was quantified by measuring the Chemical Oxygen Demand (COD) at free pH in the presence of 1 $g.L^{-1}$ of the 5In-ZnO and under UV- light irradiation (λ = 365 nm). The results presented in figure 15 display that the time required for complete photo –mineralization is longer than that required for CV degradation. A degradation time of 300 minutes was necessary to achieve 95% of CV removal. This observation reveal that the dye molecules of CV are not immediately mineralized, instead they are transformed into intermediate photo- products throughout the photo-decolorization process using 5In-ZnO nanoparticles [66].

Fig 15 Chemical Oxygen Demand (COD) removal efficiency of Crystal Violet (CV = 10 ppm) in the presence in the presence of 5In-ZnO = 1$g.L^{-1}$.



3.8.8 Photocatalytic process of In- doped ZnO nanocomposites

The photodegradation process of CV dye under UV- light usually involves four main steps, that are outlined schematically in figure 16 and expressed by the corresponding set of Equations (10) to (13). When a ZnO- based catalyst is illuminated with UV photon ($h\upsilon_{365}$), electrons in the valence band may gain sufficient energy to jump to the conduction band, an electron –hole pair is generated (Eq.10). Then, the photo generated charge carries (e^-/h^+) react separately on the surface of catalyst. The free electron (e^-) is captured by oxygen that leads to the formation of superoxide radicals ($O_2^{\bullet-}$) (Eq.11), while hole (h^+) react with adsorbed water molecules, generating highly reactive hydroxyl radicals (•OH) (Eq. 12). These both generated radicals interact efficiently with the CV dye molecules through redox reaction, resulting in their mineralization into less toxic inorganic products (Eq. 13). However, since the In- impurity is incorporated into ZnO lattice, new allowed intermediate-energy level is introduced within the forbidden band gap, which greatly enhances the separation of generated charge carries (e^-/h^+ pair), minimizes their recombination and ensure a high photo-degradation of the CV.

The carrier generation by incident light (UV- Irradiation).

$$\mathrm{In\,ZnO} + UV\ Irradiation\ (h\upsilon_{365}) \rightarrow h_{VB}^{+} + e_{CB}^{-} \quad (10)$$

Then, the reactive species formation (superoxide (O2•-) and hydroxyl (HO•) radicals

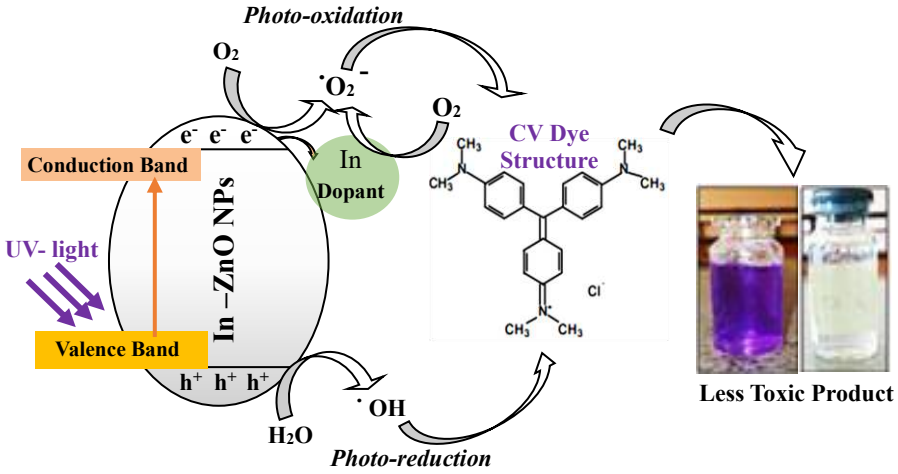
$$e_{CB}^{-} + O_2 \rightarrow O_2^{\bullet -} \quad (11)$$

$$h_{VB}^{+} + H_2O \rightarrow OH^{\bullet} + H^{+} \quad (12)$$

Finally, redox reactions lead to CV degradation and obtained non-toxic products

$$\frac{O_2^{\bullet -}}{OH^{\bullet}} + CV \rightarrow H_2O + CO_2 \quad (13)$$

Fig 16 Proposed mechanism of the CV photodegradation under UV irradiation for 5IZO-NCs synthesized from *Artemisia herba Albat* extract.



4 Conclusions

In this paper, pure and 5*a*t. % In-doped ZnO nanoparticles were successfully bio-synthesized using *Artemisia vulgaris* extract as a reducing and capping agent. In order to study the Indium In- effect addition on the structural, morphological, optical, magnetic properties as well as the photocatalytic degradation of CV dye under UV- irradiation, several characterization techniques are used including X-RD, FTIR, Raman spectroscopy, SEM-EDX, TEM, UV-Visible, PL spectroscopy, and VSM. Structurally, XRD, FTIR and Raman spectroscopy analysis results confirmed that the crystalline phase in both the P-ZnO and the 5In-ZnO nanocomposites only consists of hexagonal wurtzite. Morphologically, the crystallites size decrease from 57 to 53 nm after the In- atoms incorporation into the ZnO structure with heterogeneous grain shape of irregular agglomerate particles. Optically, on one hand, the absorbance spectra indicated a reduction in the band gap energy from 3.24 to 3.22 eV when In- atoms being incorporated. On the other hand, the PL spectra displayed two characteristic emission peaks. The visible peak emission at 568 nm in the PL spectrum of 5In-ZnO is stronger compared to that of P-ZnO located at 566 nm, which indicates an increase in the point defects concentration when In- atoms are incorporated. These point defects magnetically induce a weak ferromagnetism for both prepared nanocomposites with remanent magnetization (Mr) of 0.0025 emu/g followed by 0.0018 emu/g, respectively, and a saturation magnetization (Ms) of 0.0429 emu/g followed by 0.0343 emu/g. The photocatalytic activity of CV was studied using 5In-ZnO under UV-irradiation ($\lambda = 365$nm). The reaction kinetics indicate that CV is completely degraded after 25 min of irradiation. The higher degradation rate 99,9% is occurred at a lower dye concentration (10ppm) of CV dye. The 100% removal efficiency has been attained in 20 min under sunlight

compared to 90% under UV irradiation. The mineralization reached 95% based on COD after 300 min of irradiation.

5. References

1. H. Kaur, A. Sharma, K. Anand, A. Panday, S. Tagotra, S. Kakran, A.K. Singh, M.W. Alam, S. Kumar, B. Gassoumi, J. Dalal, G. Singh, Green synthesis of ZnO nanoparticles using E. cardamomum and zinc nitrate precursor: a dual-functional material for water purification and antibacterial applications. RSC Adv. 15, (2025). https://doi.org/10.1039/D5RA01469G

2. K.A. Malebadi, L. Sawunyama, N.H. Seheri, C. Amairia, D.C. Onwudiwe, Photocatalytic degradation of methyl orange using biogenic Ag–ZnO nanostructures derived from Searsia lancea. Appl. Phys. A 132, 170 (2026). https://doi.org/10.1007/s00339-026-09355-y

3. B.J. Singh, A. Chakraborty, R. Sehgal, A systematic review of industrial wastewater management: evaluating challenges and enablers. J. Environ. Manage. 348, 119230 (2023). https://doi.org/10.1016/j.jenvman.2023.119230

4. R.E. Palma-Goyes, F.L. Guzmán-Duque, G. Peñuela, I. González, J.L. Nava, R.A. Torres-Palma, Electrochemical degradation of crystal violet with BDD electrodes: Effect of electrochemical parameters and identification of organic by-products. Chemosphere 81, 26–32 (2010). https://doi.org/10.1016/j.chemosphere.2010.07.020

5. L. Arou, S. Madani, I. Bousnoubra, A. Boublia, I. Lakikza, S.I. Aouni, L. Abdelouahed, B. Ernst, M. Alam, Y. Benguerba, Enhanced degradation of crystal violet using PANI-ZnO nanocomposites: Electro-oxidation and photocatalysis studies. J. Mol. Liq. 412, 125818 (2024). https://doi.org/10.1016/j.molliq.2024.125818

6. S. Dutta, S. Adhikary, S. Bhattacharya, D. Roy, S. Chatterjee, A. Chakraborty, D. Banerjee, A. Ganguly, S. Nanda, P. Rajak, Contamination of textile dyes in aquatic environment: Adverse impacts on aquatic ecosystem and human health, and its management using bioremediation. J. Environ. Manage. 353, 120103 (2024). https://doi.org/10.1016/j.jenvman.2024.120103

7. P. Dhiman, G. Rana, A. Kumar, E.A. Dawi, G. Sharma, Rare earth doped ZnO nanoparticles as spintronics and photo catalyst for degradation of pollutants. Molecules 28, 2838 (2023). https://doi.org/10.3390/molecules28062838

8. S.F. Ahmed, M. Mofjur, S. Nuzhat, A.T. Chowdhury, N. Rafa, M.A. Uddin, Recent developments in physical, biological, chemical, and hybrid treatment techniques for removing emerging contaminants from wastewater. J. Hazard. Mater. 416, 125912 (2021). https://doi.org/10.1016/j.jhazmat.2021.125912

9. Z. Jiang, B. Liu, L. Yu, Y. Tong, M. Yan, R. Zhang, W. Han, Y. Hao, L. Shangguan, S. Zhang, Research progresses in preparation methods and applications of zinc oxide nanoparticles. J. Alloys Compd. 956, 170316 (2023). https://doi.org/10.1016/j.jallcom.2023.170316

10. S.M. Hosseini, S. Asadpour, M. Ghasemi, M. Shirani, Efficient photocatalytic activity of ZnO/GO/CuO nanocomposite with solar light for reduction of hexavalent chromium. Sci. Rep. 15, 20780 (2025). https://doi.org/10.1038/s41598-025-05790-8

11. M. Carofiglio, M. Laurenti, V. Vighetto, L. Racca, S. Barui, N. Garino, R. Gerbaldo, F. Laviano, V. Cauda, Iron-Doped ZnO Nanoparticles as Multifunctional Nanoplatforms for Theranostics. Nanomaterials 11, 2628 (2021). https://doi.org/10.3390/nano11102628

12. Y. Iqbal, A.R. Malik, T. Iqbal, M.H. Aziz, F. Ahmed, F.A. Abolaban, S.M. Ali, H. Ullah, Green synthesis of ZnO and Ag-doped ZnO nanoparticles using Azadirachta indica leaves: Characterization and their potential antibacterial, antidiabetic, and wound-healing activities. Mater. Lett. (2021). https://doi.org/10.1016/j.matlet.2021.130671

13. H. Ghaznavi, M.R. Hajinezhad, Z. Hesari, M. Shirvaliloo, S. Sargazi, S. Shahraki, E.A. Saberi, R. Sheervalilou, S. Jafarinejad, Synthesis, characterization, and evaluation of copper-doped zinc oxide nanoparticles anticancer effects: in vitro and in vivo experiments. BMC Cancer 25, 37 (2025). https://doi.org/10.1186/s12885-024-13398-w

14. J.H. Mahamud, A.B. Gemta, A.K. Hordofa, G.A. Argaw, U. Sherefedin, M. Ahmed, T.F. Hurrisa, T. Gurumurthi, Green synthesis and characterization of silver-doped ZnO nanoparticles using tobacco leaf extract: A novel hydrothermal approach for antibacterial and antifungal applications. AIP Adv. 15, 045030 (2025). https://doi.org/10.1063/5.0267701

15. K. Chettah, S. Boudjadar, B. Toubal, H. Guendouz, Evaluation of the Photocatalytic and Antimicrobial Properties of Cu-Doped ZnO Nanoparticles Synthesized by Phytochemical Methods. J. Nano Res. 87, 75–94 (2025). https://doi.org/10.4028/p-2IPJQj

16. H.P. Thi, T.T.H. Chu, M.V. Nguyen, Effective removal of atrazine pesticide residue from wastewater using transition metal-doped zinc oxide photocatalyst. J. Environ. Sci. Health B 59, 783–791 (2024). https://doi.org/10.1080/03601234.2024.2432162

17. N. Munna, R. Abdur, R. Islam, M.S. Bashar, S.F.U. Farhad, M. Kamruzzaman, S. Aziz, M.A.A. Shaikh, M. Hossain, M. Jamal, Influence of Sn doping on the optoelectronic properties of ZnO nanoparticles. Nanoscale Adv. 5, 4996–5004 (2023).
https://doi.org/10.1039/d3na00409k

18. A. Muhammed, T.G. Asere, T.F. Diriba, Photocatalytic and Antimicrobial Properties of ZnO and Mg-Doped ZnO Nanoparticles Synthesized Using Lupinus albus Leaf Extract. ACS Omega 9, 2480–2490 (2024). https://doi.org/10.1021/acsomega.3c07093

19. K. Pradeev Raj, K. Sadaiyandi, A. Kennedy, et al., Influence of Mg Doping on ZnO Nanoparticles for Enhanced Photocatalytic Evaluation and Antibacterial Analysis. Nanoscale Res. Lett. 13, 229 (2018). https://doi.org/10.1186/s11671-018-2643-x

20. M. Hasa, Q. Liu, A. Kanwal, T. Tariq, G. Mustafa, S. Batool, M. Ghorbanpour, Green synthesis and characterization of Mn doped ZnO nanocomposite for antibacterial and photocatalytic applications. Sci. Rep. 14, 7528 (2024). https://doi.org/10.1038/s41598-024-58393-0

21. A. Singh, R.C. Ahirwar, K. Borgaonkar, N. Gupta, M. Ahsan, J. Rathore, R. Rawat, Synthesis of transition-metal-doped nanocatalysts with antibacterial capabilities using a complementary green method. Molecules 28, 4182 (2023). https://doi.org/10.3390/molecules28104182

22. T.S. Saligedo, G.G. Muleta, T.W. Tsega, K.T. Tadele, Green Synthesis of Copper Oxide Nanoparticles Using Eichhornia Crassipes Leaf Extract, its Antibacterial and Photocatalytic Activities. Curr. Nanomater. 8, 58–68 (2023). https://doi.org/10.2174/2405461507666220301122316

23. P. Ahir, I.K. Maurya, R. Jain, S. Kumar, Photocatalytic and antimicrobial studies of green synthesized Dy3+ doped ZnO nanoparticles prepared from Rhododendron arboreum petal extract. Chem. Phys. Impact 8, 100461 (2024). https://doi.org/10.1016/j.chphi.2024.100461

24. R.T. Hussain, S. Afiqah, J.H. Shariffuddin, H. Abdullah, Green fabrication of Lanthanum doped Zinc Oxide Nanoparticles (La-ZnONPs) via Pineapple extract: Effects of Calcination Temperature on Photocatalytic Properties. J. Phys. Conf. Ser. 3003, 012016 (2025). https://doi.org/10.1088/1742-6596/3003/1/012016

25. W. Yang, I. Ullah, Z.G. Jiang, R.B. Neder, C.H. Zhan, Tailoring ultra-small ZnO nanoparticles through cobalt doping to enhance photocatalytic CO2 reduction. RSC Adv. 15, 11934–11941 (2025). https://doi.org/10.1039/d5ra01374g

26. S. Mourad, J.E. Ghoul, K. Khirouni, Role of indium doping on structural and electrical properties of ZnO nanoparticles prepared by sol–gel method. J. Mater. Sci. Mater. Electron. 31, 6372–6384 (2020). https://doi.org/10.1007/s10854-020-03193-1

27. A. Omidvar, Indium-doped and positively charged ZnO nanoclusters: versatile materials for CO detection. Vacuum 147, 126–133 (2018). https://doi.org/10.1016/j.vacuum.2017.10.023

28. Y. Ge, Z. Wei, Y. Li, J. Qu, B. Zu, X. Dou, Highly sensitive and rapid chemiresistive sensor towards trace nitro-explosive vapors based on oxygen vacancy-rich and defective crystallized In-doped ZnO. Sens. Actuators B Chem. 244, 983–991 (2017). https://doi.org/10.1016/j.snb.2017.01.092

29. P. Nuthongkum, P. Yansakorn, K. Chongsri, Improvement of structural, optical and electrical properties of indium-doped ZnO nanoparticles synthesized by Co-precipitation method. J. Mater. Sci. Mater. Electron. 34, 10 (2023). https://doi.org/10.1007/s10854-022-09418-9

30. E.T. Seid, F.B. Dejene, Controlled synthesis of In-doped ZnO: the effect of indium doping concentration. J. Mater. Sci. Mater. Electron. 30, 11833–11842 (2019). https://doi.org/10.1007/s10854-019-01557-w

31. K.J. Chen, F.Y. Hung, S.J. Chang, Structural Characteristic, Raman Analysis and Optical Properties of Indium-Doped ZnO Nanoparticles Prepared by Sol–Gel Method. J. Nanosci. Nanotechnol. 9, 3325–3329 (2009). https://doi.org/10.1166/jnn.2009.VC03

32. J. Josun, P. Sharma, V.K. Garg, Optical and structural behavior of hydrothermally synthesized ZnO nanoparticles at various temperatures with NaOH molar ratios. Results Opt. 14, 100601 (2024). https://doi.org/10.1016/j.rio.2023.100601

33. S. Cherif, H. Rezzaz-Yazid, S. Hemidouche, A. Farsi, S. Mostefaoui, M. Belmedani, H. Djelal, Z. Sadaoui, Comparative study on the photocatalytic efficiency of ZnO nanoparticles synthesized via chemical and eco-friendly coprecipitation methods. Ceram. Int. 51, 4737–4749 (2025). https://doi.org/10.1016/j.ceramint.2024.11.448

34. S. Modi, V.K. Yadav, R. Thakur, et al., Comparative Analysis of Morphological and Structural Properties of Zinc Oxide Nanoparticles Synthesized by Sonochemical Method and Microbial Method. Plasmonics 20, 5027–5044 (2025). https://doi.org/10.1007/s11468-024-02659-w

35. R. Gomathi, H. Suhana, Green synthesis, characterization and antimicrobial activity of zinc oxide nanoparticles using Artemisia pallens plant extract. Inorg. Nano-Met. Chem. 51, 1663–1672 (2021). https://doi.org/10.1080/24701556.2020.1852256

36. M. Aeineh, S.H. Najafian, M. Hosseinifarahi, Investigating the Phenological Stages of Essential Oil Yield and Essential Oil Compounds and Phytochemical Properties of Artemisia absinthium L. (Wormwood). Russ. J. Plant Physiol. 70, 149 (2023). https://doi.org/10.1134/S1021443723601891

37. D. Wang, L. Cui, X. Chang, D. Guan, Biosynthesis and characterization of zinc oxide nanoparticles from Artemisia annua and investigate their effect on proliferation, osteogenic differentiation and mineralization in human osteoblast-like MG-63 Cells. J. Photochem. Photobiol. B 202, 111652 (2020). https://doi.org/10.1016/j.jphotobiol.2019.111652

38. T.A. Orshiso, E.A. Zereffa, H.C.A. Murthy, T.B. Demissie, O. Pardeshi, L.S. Avhad, S. Ghotekar, Biosynthesis of Artemisia abyssinica Leaf Extract-Mediated Bimetallic ZnO−CuO Nanoparticles: Antioxidant, Anticancer, and Molecular Docking Studies. ACS Omega 8, 41039–41053 (2023). https://doi.org/10.1021/acsomega.3c01814

39. B. Toubal, K. Elkourd, R. Bouab, O. Abdelaziz, The impact of copper–cerium (Cu–Ce) addition on anatase-TiO2 nanostructured films for its inactivation of Escherichia coli and Staphylococcus aureus. J. Sol-Gel Sci. Technol. 103, 549–564 (2022). https://doi.org/10.1007/s10971-022-05763-7

40. Y. Gao, M. Arokia Vijaya Anand, V. Ramachandran, V. Karthikkumar, V. Shalini, S. Vijayalakshmi, D. Ernest, Biofabrication of Zinc Oxide Nanoparticles from Aspergillus niger, Their Antioxidant, Antimicrobial and Anticancer Activity. J. Clust. Sci. 30, 937–946 (2019). https://doi.org/10.1007/s10876-019-01551-6

41. E.N. Danial, M. Hjiri, M.S. Abdel-wahab, N.H. Alonizan, L. El Mir, M.S. Aida, Antibacterial activity of In-doped ZnO nanoparticles. Inorg. Chem. Commun. 122, 108281 (2020). https://doi.org/10.1016/j.inoche.2020.108281

42. A.M. Abd-Elnaiem, M. Rashad, T. Hanafy, N. Shaalan, Improvement of Optical Properties of Functionalized Polyvinyl Alcohol-Zinc Oxide Hybrid Nanocomposites for Wide Uv

Optoelectronic Applications. J. Inorg. Organomet. Polym. Mater. 33, 2429–2444 (2023). https://doi.org/10.1007/s10904-023-02616-w

43. S. Cimitan, S. Albonetti, L. Forni, F. Peri, D. Lazzari, Solvothermal synthesis and properties control of doped ZnO nanoparticles. J. Colloid Interface Sci. 329, 73–80 (2009). https://doi.org/10.1016/j.jcis.2008.09.060

44. S. Margueron, J. Pokorny, S. Skiadopoulou, S. Kamba, X. Liang, D.R. Clarke, Optical and vibrational properties of (ZnO)k In2O3 natural superlattice nanostructures. J. Appl. Phys. 119, 195103 (2016). https://doi.org/10.1063/1.4950789

45. M.I. Din, R. Sehar, Z. Hussain, R. Khalid, A.T. Shah, Synthesis of biodegradable semolina starch plastic films reinforced with biogenically synthesized ZnO nanoparticles. Inorg. Nano-Met. Chem. 51, 985–994 (2021). https://doi.org/10.1080/24701556.2020.1813768

46. E. Hamdy, A.A. Al-Askar, H. El-Gendi, W.M. Khamis, S.I. Behiry, F. Valentini, K.A. Abd-Elsalam, A. Abdelkhalek, Zinc oxide nanoparticles biosynthesized by Eriobotrya japonica leaf extract: Characterization, insecticidal and antibacterial properties. Plants 12, 2826 (2023). https://doi.org/10.3390/plants12152826

47 H. Fukushima, H. Uchida, H. Funakubo, T. Katoda, K. Nishida, Evaluation of oxygen vacancies in ZnO single crystals and powders by micro-Raman spectroscopy. J. Ceram. Soc. Jpn. 125, 445–448 (2017). https://doi.org/10.2109/jcersj2.16262

48. Y. Liu, H. Zhang, X. Ann, C. Gao, Z. Zhang, J. Zhou, J. Alloys Compd. 506, 772 (2010). https://doi.org/10.1016/j.jallcom.2010.07.067

49. Y.B. Waghadkar, G. Umarji, S.S. Kekade, S. Rane, R. Chauhan, M. Ashokkumar, S.W. Gosavi, Synthesis and characterization of indium-doped ZnO nanoparticles by coprecipitation method for highly photo-responsive UV light sensors. Sens. Int. 5, 100271 (2024). https://doi.org/10.1016/j.sintl.2023.100271

50. P.R. Jubu, O. Obaseki, A. Nathan-Abutu, F. Yam, Y. Yusof, M. Ochang, Dispensability of the Conventional Tauc's Plot for Accurate Bandgap Determination from Uv–Vis Optical Diffuse Reflectance Data. Results Opt. 9, 100273 (2022). https://doi.org/10.1016/j.rio.2022.100273

51. Y. Yu, B. Yao, Y. He, B. Cao, W. Ma, L. Chang, Oxygen defect-rich In-doped ZnO nanostructure for enhanced visible light photocatalytic activity. Mater. Chem. Phys. 244, 122672 (2020). https://doi.org/10.1016/j.matchemphys.2020.122672

52. P. Bancheva-Koleva, V. Zhelev, P. Petkov, T. Petkova, Indium-Doped ZnO Thin Films Obtained Using Spray Pyrolysis for Position-Sensitive Photodetection. Materials 18, 3744 (2025). https://doi.org/10.3390/ma18163744

53. K. Mahmood, S.B. Park, H.J. Sung, Enhanced photoluminescence, Raman spectra and field emission behavior of indium-doped ZnO nanostructures. J. Mater. Chem. C 1, 3138–3149 (2013). https://doi.org/10.1039/C7TC90063E

54. Z. Wang, Y. Zhao, J. Yang, First principles study of the electronic structure and magnetism of oxygen-deficient anatase TiO_2 (0 0 1) surface. Appl. Surf. Sci. 292, 475–479 (2014). https://doi.org/10.1016/j.apsusc.2013.11.165

55. B. Qi, S. Ólafsson, H.P. Gíslason, Vacancy defect-induced d0 ferromagnetism in undoped ZnO nanostructures: Controversial origin and challenges. Prog. Mater. Sci. 90, 45–74 (2017). https://doi.org/10.1016/j.pmatsci.2017.07.002

56. A. Sundaresan, R. Bhargavi, N. Rangarajan, U. Siddesh, C.N.R. Rao, Ferromagnetism as a universal feature of nanoparticles of the otherwise nonmagnetic oxides. Phys. Rev. B 74, 161306 (2006). https://doi.org/10.1103/PhysRevB.74.161306

57. M.H. da Silva Ribeiro, G.N. Marques, A.J. Moreira, M.M. Oliveira, R.C. Oliveira, R.T. da Silva, A.C. Krohling, W.A.A. Macedo, M.I.B. Bernardi, L.H. Mascaro, J.H.G. Rangel, H.B. de Carvalho, Green-assisted synthesis of highly defective nanostructured Fe-doped SnO2: Magnetic and photocatalytic properties evaluation. Acta Mater. 277, 120194 (2024). https://doi.org/10.1016/j.actamat.2024.120194

58. C. Staudinger, J. Breininger, I. Klimant, S.M. Borisov, Near-infrared fluorescent aza-BODIPY dyes for sensing and imaging of pH from the neutral to highly alkaline range. Analyst 144, 2393 (2019). https://doi.org/10.1039/c9an00118b

59. V. Rakić, N.P. Ulrih, Influence of pH on color variation and stability of cyanidin and cyanidin 3-O-β-glucopyranoside in aqueous solution. CyTA J. Food 19, 174–182 (2021). https://doi.org/10.1080/19476337.2021.1874539

60. M. Benamara, K.I. Nassar, M. Essid, S. Frick, J.P.B. Silva, Visible light-driven removal of Rhodamine B using indium-doped ZnO. J. Sol-Gel Sci. Technol. 111, 553–565 (2024). https://doi.org/10.1007/s10971-024-06471-0

61. N. Sedefoglu, K. Veryer, D. Zalaoglu, F. Bozok, Antibacterial and photocatalytic performances of bioactive In-doped ZnO nanoparticles. Mater. Sci. Eng. B 313, 117914 (2025). https://doi.org/10.1016/j.mseb.2024.117914

62. K. Pradeev Raj, K. Sadaiyandi, A. Kennedy, Photocatalytic and antibacterial studies of indium-doped ZnO nanoparticles synthesized by co-precipitation technique. J. Mater. Sci. Mater. Electron. 28, 19025–19037 (2017). https://doi.org/10.1007/s10854-017-7857-7

63. R. Chauhan, M. Shinde, Y. Sethi, Y. Waghadkar, S. Rondiya, N.Y. Dzade, M. Muddassir, Indium-doped ZnO as efficient photosensitive material for sunlight driven hydrogen generation and DSSC applications: integrated experimental and computational approach. J. Solid State Electrochem. 25, (2021). https://doi.org/10.1007/s10008-021-04999-7

64. K.H. Prasad, S. Vinoth, V. Ganesh, R. Ade, I.S. Yahia, Enhanced photo-sensing activity of In-doped ZnO nanoparticles synthesized by wet chemical method. Phys. B Condens. Matter 678, 415710 (2024). https://doi.org/10.1016/j.physb.2024.415710

65. D. Mahesh, J. Paul, M.C. Santhosh Kumar, Photocatalytic activity of indium doped zinc oxide seed layers and one dimensional nanorods under solar irradiation. J. Mater. Sci. Mater. Electron. 35, 1 (2024). https://doi.org/10.1007/s10854-023-11864-y

66. S. Fassi, I. Bousnobra, K. Djebbar, Synthesis of ZnO nano-particles and their application for photo-catalytic removal of dye under uv and solar energy irradiation. Environ. Eng. Manag. J. 22, 791–798 (2023). https://doi.org/10.30638/eemj.2023.062

Statements & Declarations

Funding

The authors declare that no funds, grants, or other support were received during the preparation of this manuscript.

Competing Interests

The authors have no relevant financial or non-financial interests to disclose.